PHOTONICS Research

# Spiking information processing in a single photonic spiking neuron chip with double integrated electronic dendrites

Yahui Zhang,[1,2] Shuiying Xiang,[1,2,*] Xingxing Guo,[1] Yanan Han,[1] Yuechun Shi,[3] Xiangfei Chen,[4] Genquan Han,[2] and Yue Hao[2]

[1]State Key Laboratory of Integrated Service Networks, Xidian University, Xi'an 710071, China
[2]State Key Discipline Laboratory of Wide Bandgap Semiconductor Technology, Xidian University, Xi'an 710071, China
[3]Yongjiang Laboratory, Ningbo 315202, China
[4]Key Laboratory of Intelligent Optical Sensing and Manipulation, Ministry of Education, National Laboratory of Solid State Microstructures, College of Engineering and Applied Sciences, Institute of Optical Communication Engineering, Nanjing University, Nanjing 210023, China
*Corresponding author: jxxsy@126.com

Received 5 July 2023; revised 3 September 2023; accepted 29 September 2023; posted 2 October 2023 (Doc. ID 499767); published 22 November 2023

**Dendrites, branches of neurons that transmit signals between synapses and soma, play a vital role in spiking information processing, such as nonlinear integration of excitatory and inhibitory stimuli. However, the investigation of nonlinear integration of dendrites in photonic neurons and the fabrication of photonic neurons including dendritic nonlinear integration in photonic spiking neural networks (SNNs) remain open problems. Here, we fabricate and integrate two dendrites and one soma in a single Fabry–Perot laser with an embedded saturable absorber (FP-SA) neuron to achieve nonlinear integration of excitatory and inhibitory stimuli. Note that the two intrinsic electrodes of the gain section and saturable absorber (SA) section in the FP-SA neuron are defined as two dendrites for two ports of stimuli reception, with one electronic dendrite receiving excitatory stimulus and the other receiving inhibitory stimulus. The stimuli received by two electronic dendrites are integrated nonlinearly in a single FP-SA neuron, which generates spikes for photonic SNNs. The properties of frequency encoding and spatiotemporal encoding are investigated experimentally in a single FP-SA neuron with two electronic dendrites. For SNNs equipped with FP-SA neurons, the range of weights between presynaptic neurons and postsynaptic neurons is varied from negative to positive values by biasing the gain and SA sections of FP-SA neurons. Compared with SNN with all-positive weights realized by only biasing the gain section of photonic neurons, the recognition accuracy of Iris flower data is improved numerically in SNN consisting of FP-SA neurons. The results show great potential for multi-functional integrated photonic SNN chips.** 

https://doi.org/10.1364/PRJ.499767

## 1. INTRODUCTION

Neuromorphic computing, which aims to simulate the computational processes of biological neurons, has attracted significant interest in various fields, including decision-making, speech recognition, optimization, and learning [1,2]. In a biological nervous system, a typical neuron mainly consists of three parts: the dendrites, soma, and axon. It has been experimentally demonstrated that dendritic nonlinear integration of excitatory and inhibitory stimuli plays a critical role in biological neural networks and neural computation [3–5]. Therefore, incorporating the dendritic nonlinear integration into neuromorphic computation, spiking neuron, and spiking neural networks (SNNs) is highly desirable, as it can enhance the performance and efficiency of these systems.

The continued evolution of integrated chip fabricating technologies has reawakened interest for a relentless search in neuro-inspired optical information processing [6–9]. Photonic neuromorphic processers are particularly promising for a wide range of applications that are currently unreachable by conventional computing technology, due to their undeniable advantages such as low cross talk, low latency, high speed, wide bandwidth, massive parallelism, and low power consumption [10–22]. Photonic SNNs, which are based on the spike codes, exhibit the expressiveness and efficiency of analog processing while maintaining the robustness of digital communication [6,9,10,23–28]. In photonic SNNs, various tasks such as pattern recognition and logical operation have been successfully achieved [6,23–28]. In 2019, a study demonstrated the successful recognition of

patterns in an all-optical spiking neurosynaptic network consisting of four neurons and 60 synapses [23]. In 2020, the exclusive OR (XOR) classification was implemented in a photonic SNN based on InP-based integrated photonic chips [6], while in 2021, digital recognition was achieved in a photonic SNN consisting of vertical-cavity surface-emitting lasers (VCSELs) neurons and synapses [26]. Going further, the Boolean logic gates were successfully implemented in a semiconductor Fano laser [27].

As a crucial functional unit of photonic SNNs, photonic spiking neurons are of great interest to researchers due to their ability to represent and process spikes through the complex dynamics of excitation and inhibition [29–42]. Excitatory and inhibitory dynamics were reported in a VCSEL and quantum-dot mode-locked lasers by Robertson *et al.* [35,39]. In 2018, the stable propagation of inhibited spiking dynamics in VCSELs was reported [36]. In the same year, simultaneous excitatory and inhibitory dynamics were reported in a fiber-based graphene excitable laser neuron [37]. In 2019, the all-optical inhibitory dynamics based on polarization mode competition was demonstrated [38]. In 2020, excitatory dynamics was achieved in a micropillar laser, and the computing ability of single and coupled spiking micropillar lasers was also demonstrated [40]. In 2023, the excitatory dynamics was achieved based on the fabricated Fabry–Perot laser with an intracavity saturable absorber (FP-SA) neuron [9]. However, the excitatory and inhibitory dynamics have not yet been integrated nonlinearly into the integrated semiconductor laser. Additionally, the inhibitory dynamics has not yet been applied well in the photonic SNNs for improving the performance of learning and recognition.

In this work, we fabricate and integrate two dendrites and one soma into a single FP-SA neuron. The two intrinsic electrodes of the gain section and saturable absorber (SA) section in the FP-SA neuron are defined as two dendrites for two ports of stimuli reception, with one electronic dendrite receiving excitatory stimulus and the other receiving inhibitory stimulus. The stimuli received by two electronic dendrites are integrated nonlinearly into the FP-SA neuron, which generates spikes for photonic SNNs. This approach enhances information processing capability with the utilization of the SA as one dendrite to receive stimulus, creating an additional degree of freedom for information processing within a single integrated device. Furthermore, we apply the FP-SA neuron equipped with double electronic dendrites in photonic SNNs. The range of weights between presynaptic neurons and postsynaptic neurons is varied from negative to positive values because of the ability of integrating excitatory and inhibitory stimuli in FP-SA neurons. This feature helps to enhance the accuracy of recognition. The rest of the paper is organized as follows. The experimental setup and operation principle of the FP-SA neuron with double integrated electronic dendrites are described. Then, the frequency encoding and spatiotemporal encoding are investigated experimentally in the FP-SA neuron under excitatory and inhibitory stimuli. Moreover, the recognition of the Iris data set is performed numerically in the photonic SNN consisting of FP-SA neurons based on frequency and spatiotemporal encoding. Finally, the conclusion is summarized.

## 2. RESULTS AND DISCUSSION

### A. Experimental Setup and FP-SA Neuron

As shown in Fig. 1(a), in a biological nervous system, neural information processing relies heavily on the nonlinear interaction of excitatory postsynaptic potentials and inhibitory postsynaptic potentials at dendrites. The process determines the change in the somatic membrane potential and results in neural spiking [2]. Therefore, the photonic spiking neuron that can imitate this process by utilizing double dendrites for both excitatory and inhibitory stimuli is desired. In this regard, the FP-SA laser chip is fabricated and used for implementing a photonic spiking neuron.

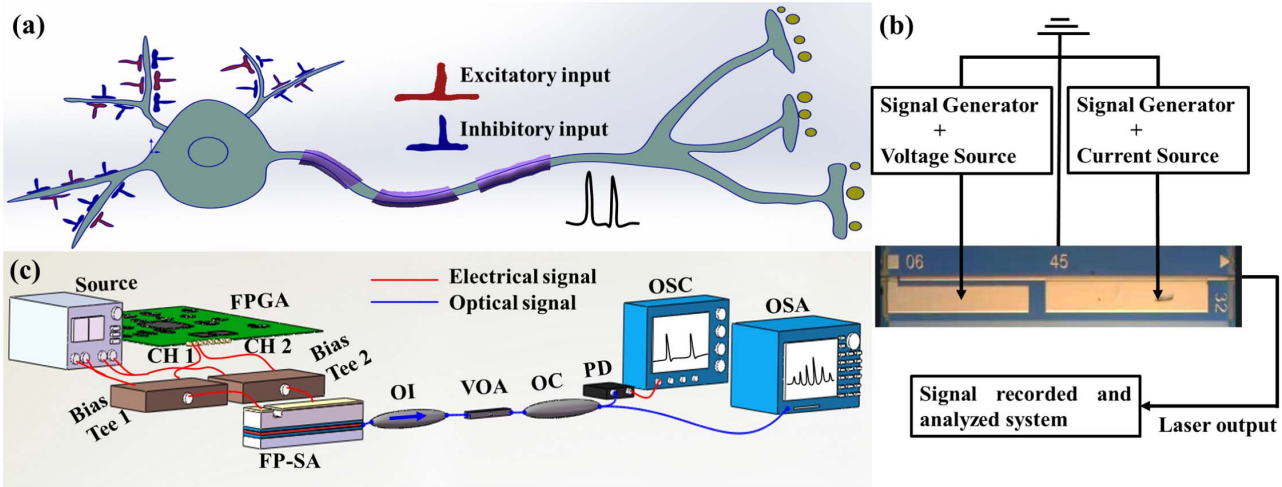


**Fig. 1.** Operation principle, chip, and experimental setup of FP-SA neuron. (a) Illustration of a biological neuron model receiving excitatory and inhibitory stimulations at functional dendrites. (b) Microscope image of the FP-SA chip and the operation principle of the FP-SA neuron. (c) Experimental setup of the encoding system based on a single FP-SA neuron with double electronic dendrites. Source, voltage source and current source; FPGA, field programmable gate array; CH1, CH2, two channels of FPGA; Bias Tee 1, Bias Tee 2, bias tees; FP-SA, integrated Fabry–Perot laser with an intracavity saturable absorber; OI, optical isolator; VOA, variable optical attenuator; OC, optical coupler; PD, photodetector; OSC, oscilloscope; OSA, optical spectrum analyzer. Red line, electrical signal; blue line, optical signal.

The microscope view of the FP-SA chip is shown in Fig. 1(b). Two electrodes of the gain section and SA section are integrated into a single FP-SA chip as two dendrites to receive excitatory and inhibitory stimuli, respectively. Then, excitatory and inhibitory stimuli are integrated nonlinearly into an FP-SA chip to generate spikes for a photonic SNN. Essentially, this single photonic neuron features double integrated electronic dendrites. In a photonic SNN, the gain section of FP-SA is biased by a current source, while the SA section is reversely biased by a voltage source. The stimuli generated by signal generators are combined with current and voltage sources with bias tees. The outputs of the FP-SA neuron are then detected, recoded, and analyzed. Further details regarding the fabrication of the FP-SA chip can be found in Ref. [9].

The schematic diagram of the experimental setup for testing the spiking encoding properties of the FP-SA neuron with double integrated electronic dendrites is displayed in Fig. 1(c). The packaged FP-SA chip is utilized as a photonic spiking neuron in the photonic SNN. The working temperature of the FP-SA is controlled at 25°C by a temperature controller (ILX Lightwave LDC-3724C). Two distinct electrical signals, generated from two channels (CH2, CH1) of FPGA (Xilinx Zynq UltraScale+ RFSoC zu48dr), are considered as excitatory and inhibitory stimuli for the gain and SA sections, which are respectively combined with the current source and voltage source through two bias tees (Bias Tee 2, Bias Tee 1). To prevent unwanted light reflections that might cause spurious results, an optical isolator (OI) is included after the FP-SA. A variable optical attenuator (VOA) is used after the OI to adjust the strength of the light signal for both the photodetector (PD) and optical spectrum analyzer (OSA, Advantest Q8384). A 50:50 optical coupler (OC) is employed to split the light signal into two paths. The first path is connected to the PD to convert the optical input signal into electrical signal, which can be recorded by an oscilloscope (OSC, Keysight DSOV334A). The second path directly feeds into an OSA. The threshold of the FP-SA for emission is approximately $I_G = 30$ mA with a reverse voltage of $V_{SA} = 0$ V. The threshold slightly increases with decreasing reverse voltage.

### B. Experimental Frequency Encoding and Spatiotemporal Encoding Mechanism in an FP-SA Neuron with Double Electrical Dendrites

The FP-SA neuron is a multiple longitudinal laser. With appropriate bias current $I_G$ and reverse voltage $V_{SA}$, the optical spectra of free-running FP-SA are depicted in Fig. 2(a) corresponding to continuous-wave and spike dynamics. The optical spectrum for the continuous-wave state is displayed in Fig. 2(a1), whereas the optical spectrum broadens for the $Q$-switching spike state as shown in Fig. 2(a2). The $Q$-switching spikes, with a full width at half maximum being about 15 ps, are depicted in Fig. 2(b). The spikes with frequencies of 2.11 GHz, 2.38 GHz, and 2.48 GHz, are generated experimentally by the FP-SA neuron with $I_G = 91$ mA, 100 mA, and 100 mA and $V_{SA} = -3.6$ V, $-3.6$ V, and $-3.8$ V, respectively. That is to say, with the same $V_{SA}$, the frequency of spikes is increased with the increase of $I_G$. In contrast, with the same $I_G$, the

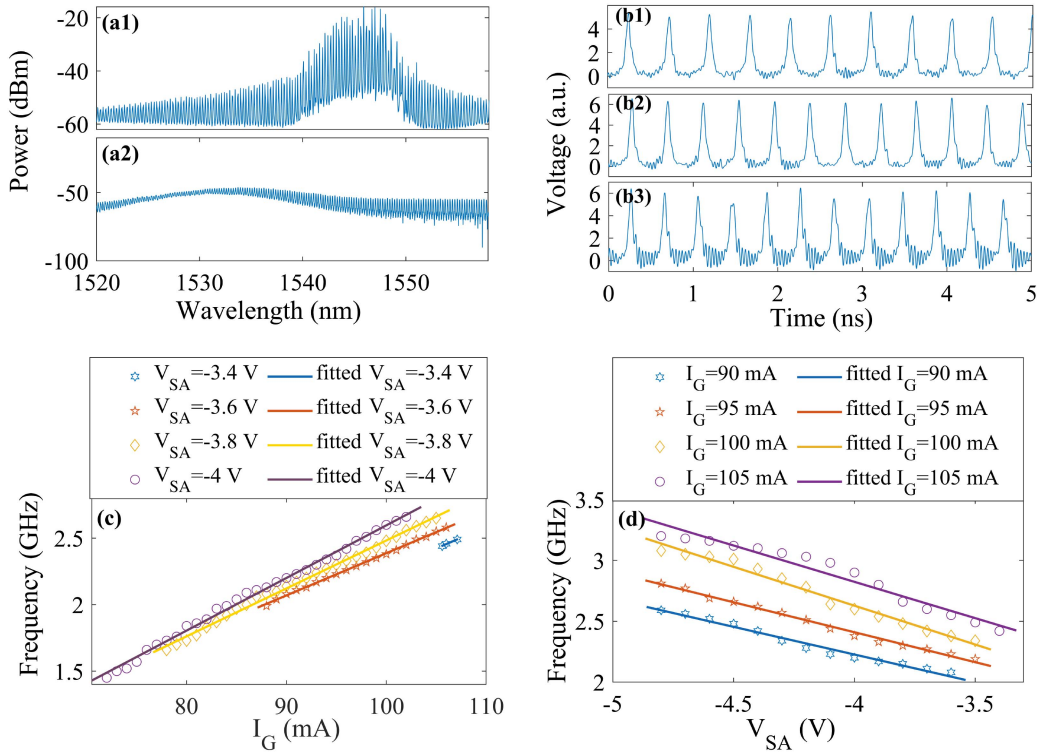


**Fig. 2.** Optical spectra and spiking dynamics of the FP-SA neuron. (a) Optical spectra of the FP-SA neuron. (a1) Optical spectrum with $I_G = 50$ mA, $V_{SA} = 0$ V; (a2) optical spectrum with $I_G = 91$ mA, $V_{SA} = -3.8$ V. (b) Spikes generated by the FP-SA neuron. (b1) $I_G = 91$ mA, $V_{SA} = -3.6$ V; (b2) $I_G = 100$ mA, $V_{SA} = -3.6$ V; (b3) $I_G = 100$ mA, $V_{SA} = -3.8$ V. (c), (d) Frequencies as functions of $I_G$ and $V_{SA}$.

frequency of spikes is increased with the decrease of $V_{SA}$. Note that for reverse bias voltage, "–" and "3.6 V" are one value. For instance, we consider that the value of "–3.8 V" is less than the value of "–3.6 V." Furthermore, the frequencies of spikes as functions of $I_G$ and $V_{SA}$ are shown in Figs. 2(c) and 2(d), respectively. It can be seen that the frequency of spikes is increased with the increase of $I_G$ and the decrease of $V_{SA}$. It is the same as the results of Fig. 2(b). Specifically, in Fig. 2(c), the spike frequency ranging from 1.43 GHz to 2.73 GHz can be achieved experimentally. Besides, the region of $I_G$ for spikes is increased with the decrease of $V_{SA}$ to some extent. For instance, the ranges of $I_G$ are about 2 mA, 18 mA, 31 mA, and 37 mA with the $V_{SA}$ of –3.4 V, –3.6 V, –3.8 V, and –4 V, respectively. Out of the region of spikes, the continuous-wave is generated by the FP-SA neuron. Thus, in Figs. 2(c) and 2(d), the bound of the continuous-wave and spike dynamics is presented. In Fig. 2(d), the spike frequency ranging from 2.01 GHz to 3.34 GHz is achieved experimentally. To avoid damage to the laser, we consider the range of $V_{SA}$ from 0 V to –4.8 V. The regions of $V_{SA}$ for spikes are similar for different considered $I_G$. For example, the ranges of $V_{SA}$ are about 1.5 V with the bias current $I_G = 90$ mA, 95 mA, 100 mA, and 105 mA. Thus, the spikes with the frequency ranging from 1.43 GHz to 3.34 GHz can be achieved experimentally in the FP-SA neuron with different $I_G$ and $V_{SA}$.

Based on the continuous-wave and spike dynamics depicted in Fig. 2, frequency encoding and spatiotemporal encoding can be achieved experimentally in the FP-SA neuron. In the region of spike dynamics, frequency encoding based on spike frequency can be achieved through controlling the bias current and voltage of the FP-SA neuron. With the switching of continuous-wave and spike dynamics, spatiotemporal encoding can be achieved in the FP-SA neuron.

Next, the frequency encoding is shown in Fig. 3. The excitatory stimulus displayed in Fig. 3(a1) is generated by channel 2 of the FPGA. Subsequently, the signal of Fig. 3(a1) is injected into the gain section of the FP-SA. There is no inhibitory stimulus applied to the FP-SA neuron as shown in Fig. 3(a2). The spike dynamics output of the FP-SA is experimentally measured and shown in Fig. 3(a3). The inset of Fig. 3(a3) indicates the enlargement of dynamics output in the red dotted box in Fig. 3(a3). It can be observed that the frequency of spikes is varying. Besides, it also can be observed that the amplitudes of the spikes fluctuate, which may be caused by white noise. We find that white noise, generated by any parts of a system including FPGA, radio frequency cable, and so on, hardly affects the frequency of spikes. To quantify the frequency of spikes generated by the FP-SA neuron, the time interval $\tau$ between spikes is measured and presented in Fig. 3(a4).

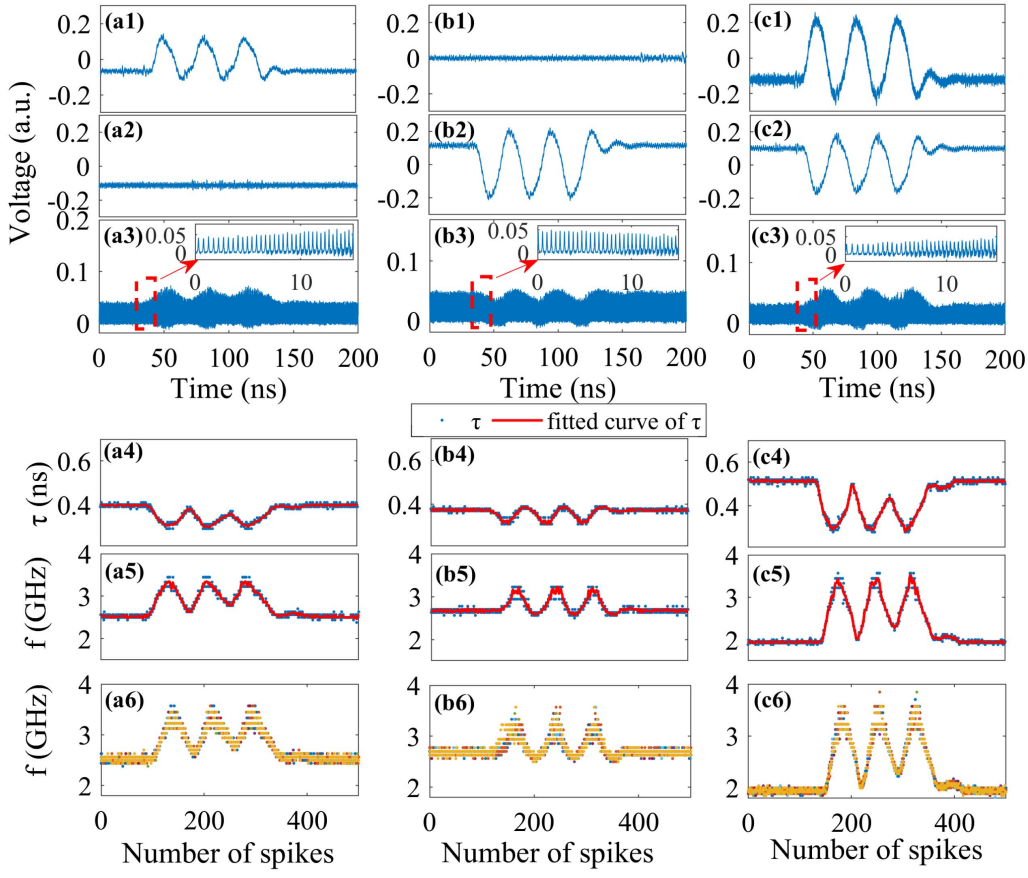


**Fig. 3.** Frequency encoding in FP-SA neuron. (a1)–(a6) Excitatory stimulus and corresponding response in FP-SA with $I_G = 90$ mA and $V_{SA} = -3.9$ V. (b1)–(b6) Inhibitory stimulus and corresponding response in FP-SA with $I_G = 90$ mA and $V_{SA} = -3.9$ V. (c1)–(c5) Simultaneous excitatory and inhibitory stimuli and corresponding response in FP-SA with $I_G = 81$ mA and $V_{SA} = -3.9$ V. (a1)–(c1) Excitatory stimulus for gain section. (a2)–(c2) Inhibitory stimulus for saturable absorber section. (a3)–(b3) Response of FP-SA neuron. (a4)–(b4) Spike time interval of spikes in (a3)–(c3). (a5)–(b5) Frequency of spikes in (a3)–(c3). (a6)–(c6) Eye diagram of (a5)–(c5).

The fitted curve of $\tau$ is also depicted in Fig. 3(a4). It is evident that there is a variation in $\tau$ from 0.3 ns to 0.4 ns, which corresponds to a change in the spike frequency $(1/\tau)$ from 3.3 GHz to 2.5 GHz, as indicated in Fig. 3(a5). Moreover, the frequency profile resembles the shape of excitatory stimulus in Fig. 3(a1). The larger the excitatory stimulus intensity is, the larger the frequency of spikes is. The frequency encoding properties are consistent with the spike dynamics properties illustrated in Fig. 2. In Fig. 3(a6), the eye diagram of the frequency sequence is depicted, where the frequencies of the spike curve overlap each other, indicating the controllable and stable frequency encoding in the FP-SA neuron. Here, the frequency of the spike curve is overlapped 10 times, making it particularly valuable for practical implementation.

The inhibitory stimuli for SA sections and their corresponding experimental responses are illustrated in Figs. 3(b1)–3(b6). It is apparent from the figures that, with a higher intensity inhibitory stimulus, the frequency of spikes is relatively lower than that with the lower intensity. For example, with the stimulus amplitude of –0.2, the frequency of spikes is approximately 3.2 GHz, while with a larger stimulus amplitude of 0.2, the frequency of spikes is roughly 2.6 GHz. These results demonstrate the inhibitory effect of stimulus in the SA section. Note that compared with Fig. 3(a3), Fig. 3(a5) and Fig. 3(b3), Fig. 3(b5), the frequency of spike is independent of its amplitude. Furthermore, the findings in Fig. 3(b6) suggest that the responses of the FP-SA under inhibitory stimulus are consistent and reproducible.

Figures 3(c1)–3(c6) experimentally demonstrate the simultaneous application of excitatory and inhibitory stimuli to the FP-SA. The nonlinear combination of these stimuli from two channels of the FPGA elicits responses in the FP-SA. For a larger excitatory stimulus paired with a smaller inhibitory stimulus, the frequency of spikes is larger. In contrast, for a smaller excitatory stimulus and a larger inhibitory stimulus, the frequency of spikes is smaller. For instance, with an excitatory stimulus amplitude of 0.25 and inhibitory stimulus amplitude of –0.17, the frequency of spikes is about 3.5 GHz, whereas, with an excitatory stimulus amplitude of 0.1 and inhibitory stimulus amplitude of –0.1, the frequency of spikes is about 1.9 GHz. Similarly, the results are controllable and stable as shown in Fig. 3(c6).

The spatiotemporal encoding is presented in Fig. 4. The excitatory and inhibitory stimuli as shown in Figs. 4(a1)–4(c2) are generated by the CH2, CH1, as well as both CH2 and CH1 of the FPGA. The responses of excitatory stimulus are presented in Fig. 4(a3). It is evident that the excitatory stimulus can trigger neuron-like spikes in the FP-SA upon the arrival of excitatory stimulus pulses. Thus, spatiotemporal encoding can be achieved in the FP-SA neuron by switching between continuous-wave and spiking dynamics.

The responses of inhibitory stimulus in Fig. 4(b2) for spatiotemporal encoding are shown in Fig. 4(b3). It can be seen that with inhibitory stimulus, spikes are inhibited in the FP-SA neuron with initial spiking dynamics. The responses of simultaneous excitatory and inhibitory stimuli are presented in Fig. 4(c3). It can be observed that the spikes triggered by excitatory stimulus are inhibited by the inhibitory stimulus, exhibiting properties similar to the biological inhibition. The stability property of spatiotemporal encoding is demonstrated by overlapped color maps in Figs. 4(a4)–4(c4). In these color maps, spikes are represented by colors of yellow and black,

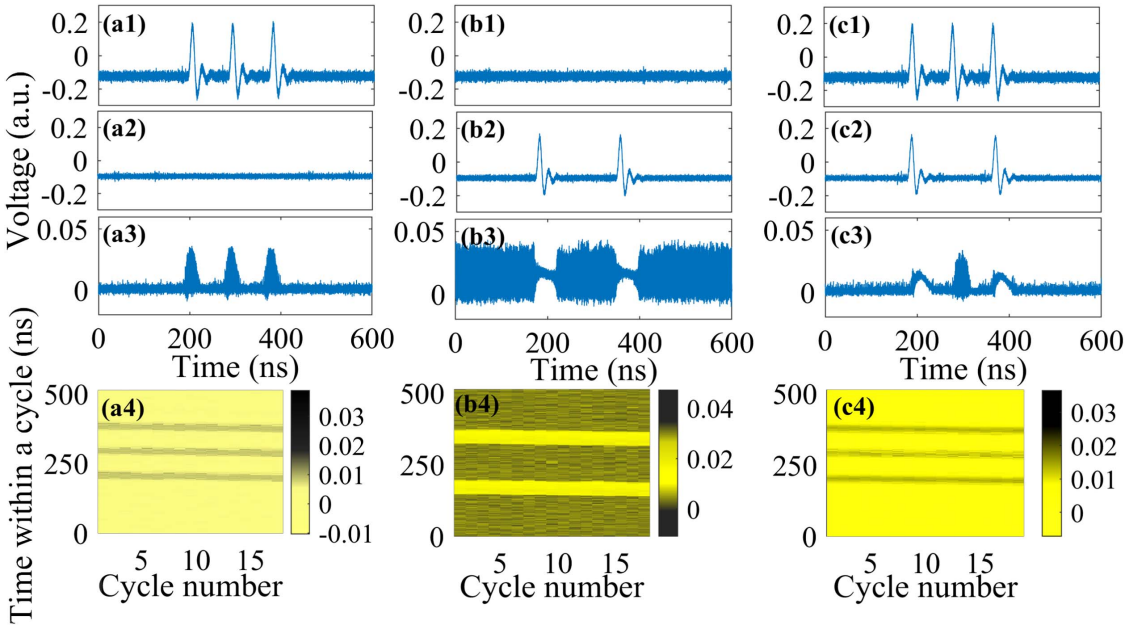


**Fig. 4.** Spatiotemporal encoding in FP-SA neuron. (a1)–(a4) Excitatory stimulus and corresponding response in FP-SA with $I_G = 65$ mA and $V_{SA} = -4.6$ V. (b1)–(b4) Inhibitory stimulus and corresponding response in FP-SA with $I_G = 64$ mA and $V_{SA} = -4.19$ V. (c1)–(c4) Simultaneous excitatory and inhibitory stimuli and corresponding response in FP-SA with $I_G = 61.6$ mA and $V_{SA} = -3.97$ V. (a1)–(c1) Excitatory stimulus for gain section. (a2)–(c2) Inhibitory stimulus for saturable absorber section. (a3)–(b3) Response of FP-SA neuron. (a4)–(b4) Overlapped color map of the responses of FP-SA neuron.

whereas the continuous-wave is represented by consistent yellow or consistent black. It can be seen that the results of all three cases are stable and controllable. Thus, Fig. 4 effectively demonstrates the spatiotemporal encoding properties of a single FP-SA with double integrated electronic dendrites for excitatory and inhibitory stimuli.

### C. Numerical Recognition in Photonic SNNs Consisting of FP-SA Neurons with Double Dendrites

Next, by employing the proposed FP-SA neuron with double electrical dendrites, the recognition of the Iris data set is performed numerically in two photonic SNNs based on frequency encoding and spatiotemporal encoding.

In photonic SNNs, when the presynaptic neurons are connected to the gain section of traditional photonic postsynaptic neurons, the weights between presynaptic neurons and postsynaptic neurons are all positive values due to the magnitude/intensity modulation. To expand the range of weights, we introduce the FP-SA neuron for photonic SNNs. Except for the connection to the gain section, the connection to the SA section of FP-SA postsynaptic neurons is increased. For a single FP-SA neuron, the stimulus in the SA section of the FP-SA is inhibitory stimulus, which can decrease spike frequency or inhibit triggered spikes. Similarly, in photonic SNNs, inhibitory stimuli for postsynaptic neurons are represented by the negative weights of connections between presynaptic neurons and postsynaptic neurons. Thus, the weight range is expanded to both negative and positive values.

In the photonic SNNs based on FP-SA neurons, the model of all photonic neurons is considered as the Yamada model of a two-section laser [43]. The model is rewritten as follows:

$$\frac{dN_{ph}}{dt}=\Gamma_G g_G(n_G-n_{0G})N_{ph}+\Gamma_{SA}g_{SA}(n_{SA}-n_{0SA})N_{ph} -\frac{N_{ph}}{\tau_{ph}}+V_{oG}\beta B_r n_G^2, \tag{1}$$

$$\frac{dn_{iSA}}{dt}=-\Gamma_{iSA}g_{iSA}(n_{iSA}-n_{0iSA})\frac{N_{iph}}{V_{oiSA}}-\frac{n_{iSA}}{\tau_{iSA}}+\frac{I_{iSA}+i_i(t)}{eV_{oiSA}}, \tag{2}$$

$$\frac{dn_{jSA}}{dt}=-\Gamma_{jSA}g_{jSA}(n_{jSA}-n_{0jSA})\frac{N_{jph}}{V_{ojSA}}-\frac{n_{jSA}}{\tau_{jSA}} +\frac{I_{jSA}+\eta_{cij}\sum_{i=1}^{n_{pre}}\omega_{ij}P_i(t-\tau_r)}{eV_{ojSA}}, \tag{3}$$

$$\frac{dn_{iG}}{dt}=-\Gamma_{iG}g_{iG}(n_{iG}-n_{0iG})\frac{N_{iph}}{V_{oiG}}-\frac{n_{iG}}{\tau_{iG}}+\frac{I_{iG}+i_e(t)}{eV_{oiG}}, \tag{4}$$

$$\frac{dn_{jG}}{dt}=-\Gamma_{jG}g_{jG}(n_{jG}-n_{0jG})\frac{N_{jph}}{V_{ojG}}-\frac{n_{jG}}{\tau_{jG}} +\frac{I_{jG}+\eta_{cij}\sum_{i=1}^{n_{pre}}\omega_{ij}P_i(t-\tau_r)}{eV_{ojG}}, \tag{5}$$

$$P(t)\approx\frac{\eta_c\Gamma_G}{\tau_{ph}}\frac{hc}{\lambda}N_{ph}(t), \tag{6}$$

where the subscript $i$ in Eqs. (2), (4) and subscript $j$ in Eqs. (3), (5) respectively represent the indices of presynaptic neurons and postsynaptic neurons in Fig. 5. Thus, the Yamada model of presynaptic neurons is represented in Eqs. (1), (2), (4), and (6). The model of postsynaptic neurons is represented in Eqs. (1), (3), (5), and (6). The subscripts $G$ and SA denote the gain and SA sections of the FP-SA. $N_{ph}$ represents the total photon number in the cavity, $n_G(t)$ [$n_{SA}(t)$] is the carrier density in the gain (SA) sections, and $P(t)$ is the output power of the FP-SA. The stimuli of presynaptic FP-SA neurons in the form of $i_i(t)$ and $i_e(t)$ are introduced in Eqs. (2) and (4) for SA and gain sections, respectively. The stimuli for SA and gain sections of postsynaptic FP-SA neurons are $\eta_{cij}\sum_{i=1}^{n_{pre}}\omega_{ij}P_i(t-\tau_r)$, where $\omega_{ij}$ and $\tau_r$ are coupling weight and coupling delay between presynaptic neurons and postsynaptic neurons, respectively. $n_{pre}$ is the number of presynaptic neurons. $\eta_{cij}$ is the coupling coefficient from presynaptic neurons to postsynaptic neurons. Here, when $\omega_{ij}$ is in the range of [0, 1] ([−1, 0]), $\omega_{ij}$ in Eq. (3) [Eq. (4)] is set to zero. Other parameters are the bias current in the gain (SA) region $I_G$ ($I_{SA}$) and the lasing wavelength for FP-SA $\lambda$ (850 nm for all lasers). Other device parameters described and summarized in Table 1 are considered to be identical for all FP-SA neurons. We numerically solve Eqs. (1)–(5) by using parameters for FP-SA neurons: $I_G=2$ mA, $I_{SA}=0$ mA, and $\tau_r=2$ ns.

The sample number of the Iris data set is considered as 150. Here, we compared the recognition accuracy of the Iris data set in neural networks with the same architecture but different weight limitations. In one case, the weights are limited to positive values under the condition of the only connection to the

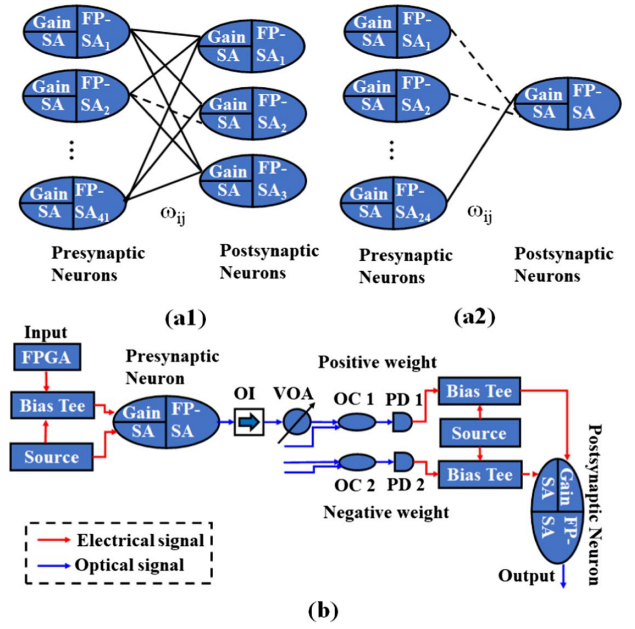


**Fig. 5.** Schematic diagram of photonic SNN for the recognition of Iris data set. (a1) Photonic SNN based on frequency encoding. (a2) Photonic SNN based on spatiotemporal encoding. (b) Detailed connection of presynaptic neuron and postsynaptic neuron.

**Table 1. Two-Section Laser Parameters**

| Param. | Description | Value |
|---|---|---|
| $V_G$ | Gain section cavity volume | $2.4 \times 10^{-18}$ m$^3$ |
| $V_{SA}$ | SA section cavity volume | $2.4 \times 10^{-18}$ m$^3$ |
| $\Gamma_G$ | Gain section confinement factor | 0.06 |
| $\Gamma_{SA}$ | SA section confinement factor | 0.05 |
| $\tau_G$ | Gain section carrier lifetime | 1 ns |
| $\tau_{SA}$ | SA section carrier lifetime | 100 ps |
| $\tau_{ph}$ | Photon lifetime | 4.8 ps |
| $g_G$ | Gain section differential gain/loss | $2.9 \times 10^{-12}$ m$^3$ s$^{-1}$ |
| $g_{SA}$ | SA section differential gain/loss | $14.5 \times 10^{-12}$ m$^3$ s$^{-1}$ |
| $n_{0G}$ | Gain section transparency carrier density | $1.1 \times 10^{24}$ m$^{-3}$ |
| $n_{0SA}$ | SA section transparency carrier density | $0.89 \times 10^{24}$ m$^{-3}$ |
| $B_r$ | Bimolecular recombination term | $10 \times 10^{-16}$ m$^3$ s$^{-1}$ |
| $\eta_c$ | Output power coupling coefficient | 0.4 |
| $\beta$ | Spontaneous emission coupling factor | $1 \times 10^{-4}$ |
| $c$ | Speed of light | $3 \times 10^8$ m/s |
| $h$ | Planck constant | $6.63 \times 10^{-34}$ J s |
| $e$ | Electron charge | $1.6 \times 10^{-19}$ C |

gain section of postsynaptic neurons, while in another case, the weights can range from negative to positive values due to the FP-SA postsynaptic neurons. That is to say, the range of weights is [0, 1] with all connections to the gain section, while the range of weights is [−1, 1] with networks consisting of FP-SA neurons with double electrical dendrites.

For the case of the [−1, 1] weight range, based on the frequency encoding in FP-SA neurons, the schematic diagram of a network for the recognition of the Iris data set is shown in Fig. 5(a1). A single-layer fully connected neural network consisting of 41 presynaptic neurons and three postsynaptic neurons is presented [43]. The weights between the presynaptic neuron and postsynaptic neuron are represented by $\omega_{ij}$. The Iris data set inputs are converted to the frequency of spikes by presynaptic neurons. The recognition results are represented by the frequency of spikes generated by postsynaptic neurons. As illustrated in Fig. 5(a1), FP-SA neurons with double dendrites are employed as both presynaptic and postsynaptic neurons. The detailed connections of one presynaptic and one postsynaptic neuron are presented in Fig. 5(b). For the presynaptic neuron, the excitatory stimulus is combined with a direct current source through a bias tee to bias the gain section. The outputs of the presynaptic neuron are injected into one port of OC 1 through OI and VOA. The OI is used to avoid unwanted reflected light that might affect the results of the presynaptic FP-SA neuron. The VOA is included to adjust the weight value between the connected presynaptic neuron and postsynaptic neuron according to the training. OC 1 is used to combine different weighted presynaptic neuron outputs in a weight range of [0, 1]; meanwhile, presynaptic neuron outputs corresponding to connected weights in a range of [−1, 0] are combined by OC 2. The optical signals from OC 1 and OC 2 are converted into electrical signal by PD 1 and PD 2 to bias the gain and SA sections of the postsynaptic FP-SA neuron. Then, the outputs of all presynaptic neurons are integrated nonlinearly in the postsynaptic FP-SA neuron to generate spikes for photonic SNNs. All presynaptic neurons and postsynaptic neurons in Fig. 5(a1) are connected in the way shown in Fig. 5(b).

The photonic SNN is trained by the back-propagation algorithm with all weights initialized in the range of [0, 1]. The weights of the photonic SNN are achieved based on the conversion of an artificial neural network [43]. The recognition accuracy as a function of learning cycles with two cases is shown in Fig. 6(a1). With two cases of weight ranges of [0, 1] and [−1, 1], the recognition accuracy is 98.67% and 100% in the 386th and 231st learning cycles, respectively. Therefore, based on frequency encoding, the accuracy of recognition can be enhanced by including both positive and negative weights. Specifically, the weight distributions of the two cases are displayed in Figs. 6(b1) and 6(c1), respectively.

Based on the spatiotemporal encoding in the FP-SA neuron, the network architecture with 24 presynaptic neurons and one postsynaptic neuron is shown in Fig. 5(a2). The connected details are the same as those for the case of frequency encoding, which are depicted in Fig. 5(b). The weights of the photonic SNN with spatiotemporal encoding are trained based on the ReSuMe algorithm [44], and the recognition results are represented by the spikes with different spiking timing in FP-SA neurons. The recognition accuracy in two different weight ranges as a function of learning cycles is presented in Fig. 6(b2). It can be seen that with a larger weight range of [−1, 1], the recognition accuracy also can be improved to some extent. Specifically, the achieved highest accuracy is 89% and 92% in the 327th and 372nd learning cycles with the weight ranges of [0, 1] and [−1, 1], respectively. Thus, by introducing the FP-SA neuron with double electrical dendrites, the recognition accuracy can be enhanced through expanding the weight range.

Moreover, we also consider the recognition of the Iris data set with noisy stimuli for presynaptic neurons as well as noisy spikes propagating from presynaptic neurons to postsynaptic neurons. The recognition accuracy of the Iris data set is illustrated in Fig. 7. It can be seen that, although the recognition accuracy of the Iris data set slightly decreases compared to that shown in Fig. 6, it still remains higher with the weight range of

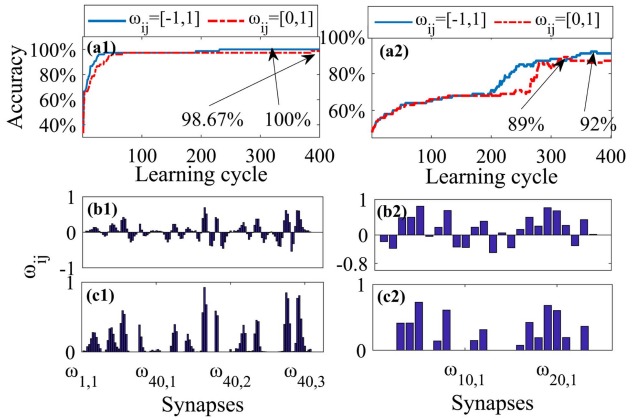


**Fig. 6.** (a1), (a2) Recognition accuracy of the Iris data set and (b1)–(c2) weight distribution of corresponding photonic SNNs. (a1)–(c1) Corresponding to the architecture of Fig. 5(a1) with the frequency encoding; (a2)–(c2) corresponding to the architecture of Fig. 5(a2) with the spatiotemporal encoding. (b1), (b2) Weight range is [−1, 1]; (c1), (c2) weight rang is [0, 1].

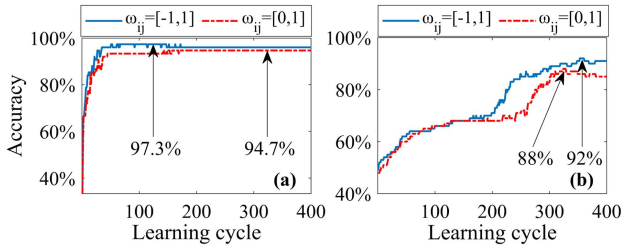


**Fig. 7.** Recognition accuracy of the Iris data set in noisy photonic SNNs. (a) Corresponding to the architecture of Fig. 5(a1) with the frequency encoding; (b) corresponding to the architecture of Fig. 5(a2) with the spatiotemporal encoding.

[−1, 1] compared to the accuracy obtained with the weight range of [0, 1] for both frequency encoding and spatiotemporal encoding schemes. To be precise, based on the frequency encoding, the accuracy reaches 97.3% and 94.7% with the weight ranges of [−1, 1] and [0, 1] respectively. On the other hand, with spatiotemporal encoding, the accuracy is 92% and 88% with the weight ranges of [−1, 1] and [0, 1], respectively. It should be noted that the discrepancy in recognition accuracy between frequency encoding and spatiotemporal encoding is due to various factors such as architectures, algorithms, and data encodings.

Thus, for both frequency encoding and spatiotemporal encoding schemes, the recognition accuracy can be enhanced based on the FP-SA neurons with double dendrites by expanding the weight range. The results are of value for the development of photonic SNNs for pattern classification.

## 3. CONCLUSION

In the present work, we demonstrate the nonlinear integration of excitatory and inhibitory stimuli in the FP-SA neuron with double integrated electronic dendrites. The electrodes of the gain section and SA section are considered as two electronic dendrites of the FP-SA photonic neuron, which increases the degree of freedom for information processing in a single integrated chip. The frequency encoding and spatiotemporal encoding are investigated in the fabricated FP-SA neuron. Moreover, we apply the FP-SA neuron equipped with double electronic dendrites in the photonic SNN, which increase the weight range to enhance the recognition accuracy. The results in the paper are valuable for the development of photonic SNN, for example, multi-functional integrated photonic SNN chips.

**Funding.** National Key Research and Development Program of China (2021YFB2801900, 2021YFB2801902, 2021YFB2801904); National Natural Science Foundation of China (61974177, 61674119, 62204196, 62205258); National Outstanding Youth Science Fund Project of National Natural Science Foundation of China (62022062); Fundamental Research Funds for the Central Universities (QTZX23041, XJS220124).

**Disclosures.** The authors declare no conflicts of interest.

**Data Availability.** Data underlying the results presented in this paper are not publicly available at this time but may be obtained from the authors upon reasonable request.

## REFERENCES

1. K. Roy, A. Jaiswal, and P. Panda, "Towards spike-based machine intelligence with neuromorphic computing," Nature **575**, 607–617 (2019).
2. W. Maass, "Networks of spiking neurons: the third generation of neural network models," Neural Netw. **10**, 1659–1671 (1997).
3. J. Hao, X. D. Wang, Y. Dan, M. M. Poo, and X. H. Zhang, "An arithmetic rule for spatial summation of excitatory and inhibitory inputs in pyramidal neurons," Proc. Natl. Acad. Sci. USA **106**, 21906–21911 (2009).
4. A. Payeur, B. Jean-Claude, and N. Richard, "Classes of dendritic information processing," Curr. Opin. Neurobiol. **58**, 78–85 (2019).
5. A. Gidon, T. A. Zolnik, P. Fidzinski, F. Bolduan, A. Papoutsi, P. Poirazi, M. Holtkamp, I. Vida, and M. E. Larkum, "Dendritic action potentials and computation in human layer 2/3 cortical neurons," Science **367**, 83–87 (2020).
6. H. T. Peng, G. Angelatos, T. F. de Lima, M. A. Nahmias, A. N. Tait, S. Abbaslou, B. J. Shastri, and P. R. Prucnal, "Temporal information processing with an integrated laser neuron," IEEE J. Sel. Top. Quantum Electron. **26**, 5100209 (2020).
7. S. Xu, J. Wang, H. Shu, Z. Zhang, S. Yi, B. Bai, X. Wang, J. Liu, and W. Zou, "Optical coherent dot-product chip for sophisticated deep learning regression," Light Sci. Appl. **10**, 221 (2021).
8. Y. Tian, Y. Zhao, S. Liu, Q. Li, W. Wang, J. Feng, and J. Guo, "Scalable and compact photonic neural chip with low learning-capability-loss," Nanophotonics **11**, 329–344 (2022).
9. S. Xiang, Y. Shi, X. Guo, Y. Zhang, H. Wang, D. Zheng, Z. Song, Y. Han, S. Gao, S. Zhao, B. Gu, H. Wang, X. Zhu, L. Hou, X. Chen, W. Zheng, X. Ma, and Y. Hao, "Hardware-algorithm collaborative computing with photonic spiking neuron chip based on integrated Fabry-Pérot laser with saturable absorber," Optica **10**, 162–171 (2022).
10. P. R. Prucnal, B. J. Shastri, T. F. de Lima, M. A. Nahmias, and A. N. Tait, "Recent progress in semiconductor excitable lasers for photonic spike processing," Adv. Opt. Photon. **8**, 228–299 (2016).
11. Y. Shen, N. C. Harris, S. Skirlo, M. Prabhu, T. Baehr-Jones, M. Hochberg, X. Sun, S. Zhao, H. Larochelle, D. Englund, and M. Soljačić, "Deep learning with coherent nanophotonic circuits," Nat. Photonics **11**, 441–446 (2017).
12. X. Lin, Y. Rivenson, N. T. Yardimci, M. Veli, Y. Luo, M. Jarrahi, and A. Ozcan, "All-optical machine learning using diffractive deep neural networks," Science **361**, 1004–1008 (2018).
13. G. Wetzstein, A. Ozcan, S. Gigan, S. Fan, D. Englund, M. Soljačić, C. Denz, D. A. B. Miller, and D. Psaltis, "Inference in artificial intelligence with deep optics and photonics," Nature **588**, 39–47 (2020).
14. W. Zou, B. Ma, S. Xu, X. Zou, and X. Wang, "Towards an intelligent photonic system," Sci. China Inf. Sci. **63**, 160401 (2020).
15. B. J. Shastri, A. N. Tait, T. F. de Lima, W. H. P. Pernice, H. Bhaskaran, C. D. Wright, and P. R. Prucnal, "Photonics for artificial intelligence and neuromorphic computing," Nat. Photonics **15**, 102–114 (2021).
16. S. Xiang, Y. Han, Z. Song, X. Guo, Y. Zhang, Z. Ren, S. Wang, Y. Ma, W. Zou, and B. Ma, "A review: photonics devices, architectures, and algorithms for optical neural computing," J. Semicond. **42**, 023105 (2021).
17. X. Guo, J. Xiang, Y. Zhang, and Y. Su, "Integrated neuromorphic photonics: synapses, neurons, and neural networks," Adv. Photon. Res. **2**, 2000212 (2021).
18. J. Feldmann, N. Youngblood, M. Karpov, H. Gehring, X. Li, M. Stappers, M. Le Gallo, X. Fu, A. Lukashchuk, A. S. Raja, J. Liu, C. D. Wright, A. Sebastian, T. J. Kippenberg, W. H. P. Pernice, and H. Bhaskaran, "Parallel convolutional processing using an integrated photonic tensor core," Nature **589**, 52–58 (2021).
19. T. K. Zhou, X. Lin, J. Wu, Y. Chen, H. Xie, Y. Li, J. Fan, H. Wu, L. Fang, and Q. Dai, "Large-scale neuromorphic optoelectronic computing with a reconfigurable diffractive processing unit," Nat. Photonics **15**, 367–373 (2021).

20. H. Zhou, J. Dong, J. Cheng, W. Dong, C. Huang, Y. Shen, Q. Zhang, M. Gu, C. Qian, H. Chen, Z. Ruan, and X. Zhang, "Photonic matrix multiplication lights up photonic accelerator and beyond," Light Sci. Appl. **11**, 30 (2022).
21. C. Huang, V. J. Sorger, M. Miscuglio, M. Al-Qadasi, A. Mukherjee, L. Lampe, M. Nichols, A. N. Tait, T. F. de Lima, B. A. Marquez, J. Wang, L. Chrostowski, M. P. Fok, D. Brunner, S. Fan, S. Shekhar, P. R. Prucnal, and B. J. Shastri, "Prospects and applications of photonic neural networks," Adv. Phys. X **7**, 1981155 (2022).
22. A. Zhao, N. Jiang, J. Peng, S. Liu, Y. Zhang, and K. Qiu, "Parallel generation of low-correlation wideband complex chaotic signals using CW laser and external-cavity laser with self-phase-modulated injection," Opto-Electron. Adv. **5**, 200026 (2022).
23. J. Feldmann, N. Youngblood, C. D. Wright, H. Bhaskaran, and W. H. P. Pernice, "All-optical spiking neurosynaptic networks with self-learning capabilities," Nature **569**, 208–214 (2019).
24. Z. Song, S. Xiang, Z. Ren, S. Wang, A. Wen, and Y. Hao, "Photonic spiking neural network based on excitable VCSELs-SA for sound azimuth detection," Opt. Express **28**, 1561–1573 (2020).
25. T. Inagaki, K. Inaba, T. Leleu, T. Honjo, T. Ikuta, K. Enbutsu, T. Umeki, R. Kasahara, K. Aihara, and H. Takesue, "Collective and synchronous dynamics of photonic spiking neurons," Nat. Commun. **12**, 2325 (2021).
26. S. Xiang, Z. Ren, Z. Song, Y. Zhang, X. Guo, G. Han, and Y. Hao, "Computing primitive of fully-VCSELs-based all-optical spiking neural network for supervised learning and pattern classification," IEEE Trans. Neural Netw. Learn. Syst. **32**, 2494–2505 (2021).
27. T. Chen, P. Zhou, Y. Huang, Y. Zeng, S. Xiang, and N. Li, "Boolean logic gates implemented by a single photonic neuron based on a semiconductor Fano laser," Opt. Contin. **1**, 1859–1866 (2022).
28. T. Makinwa, K. Inaba, T. Inagaki, Y. Yamada, T. Leleu, T. Honjo, T. Ikuta, K. Enbutsu, T. Umeki, R. Kasahara, K. Aihara, and H. Takesue, "Experimental observation of chimera states in spiking neural networks based on degenerate optical parametric oscillators," Commun. Phys. **6**, 121 (2023).
29. W. Coomans, L. Gelens, S. Beri, J. Danckaert, and G. Van der Sande, "Solitary and coupled semiconductor ring lasers as optical spiking neurons," Phys. Rev. E **84**, 036209 (2011).
30. A. Hurtado, K. Schires, I. D. Henning, and M. J. Adams, "Investigation of vertical cavity surface emitting laser dynamics for neuromorphic photonic systems," Appl. Phys. Lett. **100**, 103703 (2012).
31. F. Selmi, R. Braive, G. Beaudoin, I. Sagnes, R. Kuszelewicz, and S. Barbay, "Relative refractory period in an excitable semiconductor laser," Phys. Rev. Lett. **112**, 183902 (2014).
32. B. J. Shastri, M. A. Nahmias, A. N. Tait, A. W. Rodriguez, B. Wu, and P. R. Prucnal, "Spiking processing with a graphene excitable laser," Sci. Rep. **6**, 19126 (2016).
33. T. Deng, J. Robertson, and A. Hurtado, "Controlled propagation of spiking dynamics in vertical-cavity surface-emitting lasers: towards neuromorphic photonic networks," IEEE J. Sel. Top. Quantum Electron. **23**, 1800408 (2017).
34. I. Chakraborty, G. Saha, G. Sengupta, and K. Roy, "Toward fast neural computing using all-photonic phase change spiking neurons," Sci. Rep. **8**, 12980 (2018).
35. J. Robertson, T. Ackemann, L. F. Lester, and A. Hurtado, "Externally-triggered activation and inhibition of optical pulsating regimes in quantum-dot mode-locked lasers," Sci. Rep. **8**, 12515 (2018).
36. T. Deng, J. Robertson, Z. Wu, G. Xia, X. Lin, X. Tang, Z. Wang, and A. Hurtado, "Stable propagation of inhibited spiking dynamics in vertical-cavity surface-emitting lasers for neuromorphic photonic networks," IEEE Access **6**, 67951–67958 (2018).
37. P. Y. Ma, B. J. Shastri, T. F. de Lima, C. Huang, A. N. Tait, M. A. Nahmias, H.-T. Peng, and P. R. Prucnal, "Simultaneous excitatory and inhibitory dynamics in an excitable laser," Opt. Lett. **43**, 3802–3805 (2018).
38. Y. Zhang, S. Xiang, X. Guo, A. Wen, and Y. Hao, "All-optical inhibitory dynamics in photonic neuron based on polarization mode competition in a VCSEL with an embedded saturable absorber," Opt. Lett. **44**, 1548–1551 (2019).
39. J. Robertson, E. Wade, Y. Kopp, Y. Bueno, and A. Hurtado, "Toward neuromorphic photonic networks of ultrafast spiking laser neurons," IEEE J. Sel. Top. Quantum Electron. **26**, 7700715 (2020).
40. V. A. Pammi, K. Alfaro-Bittner, M. G. Clerc, and S. Barbay, "Photonic computing with single and coupled spiking micropillar lasers," IEEE J. Sel. Top. Quantum Electron. **26**, 1500307 (2020).
41. A. Jha, C. Huang, H.-T. Peng, B. Shastri, and P. R. Prucnal, "Photonic spiking neural networks and graphene-on-silicon spiking neurons," J. Lightwave Technol. **40**, 2901–2914 (2022).
42. J. Xiang, Y. Zhang, Y. Zhao, X. Guo, and Y. Su, "All-optical silicon microring spiking neuron," Photon. Res. **10**, 939–946 (2022).
43. Y. Han, S. Xiang, T. Zhang, Y. Zhang, X. Guo, Y. Shi, and Y. Hao, "Conversion of a single-layer ANN to photonic SNN for pattern recognition," Sci. China Inf. Sci. (2023).
44. F. Ponulak and A. Kasiński, "Supervised learning in spiking neural networks with ReSuMe: sequence learning, classification, and spike shifting," Neural Comput. **22**, 467–510 (2010).